The stellar wind cycles and planetary radio emission of the τ Boo system

A. A. Vidotto,[1]★ R. Fares,[1] M. Jardine,[1] J.-F. Donati,[2] M. Opher,[3] C. Moutou,[4] C. Catala[5] and T. I. Gombosi[6]

[1]*SUPA, School of Physics and Astronomy, University of St Andrews, North Haugh, St Andrews KY16 9SS*
[2]*LATT-UMR 5572, CNRS & Univ. P. Sabatier, 14 Av. E. Belin, F-31400 Toulouse, France*
[3]*Department of Astronomy, Boston University, 725 Commonwealth Avenue, Boston, MA 02215, USA*
[4]*LAM-UMR 6110, CNRS & Univ. de Provence, 38 rue Fréderic Juliot-Curie, F-13013 Marseille, France*
[5]*LESIA-UMR 8109, CNRS & Univ. Paris VII, 5 Place Janssen, F-92195 Meudon Cedex, France*
[6]*Department of Atmospheric, Oceanic and Space Sciences, University of Michigan, 1517 Space Research Building, Ann Arbor, MI 48109, USA*

ABSTRACT

τ Boo is an intriguing planet-host star that is believed to undergo magnetic cycles similar to the Sun, but with a duration that is about one order of magnitude smaller than that of the solar cycle. With the use of observationally derived surface magnetic field maps, we simulate the magnetic stellar wind of τ Boo by means of three-dimensional magnetohydrodynamics numerical simulations. As the properties of the stellar wind depend on the particular characteristics of the stellar magnetic field, we show that the wind varies during the observed epochs of the cycle. Although the mass-loss rates we find ($\sim 2.7 \times 10^{-12}\,M_\odot\,yr^{-1}$) vary less than 3 per cent during the observed epochs of the cycle, our derived angular-momentum-loss rates vary from 1.1 to 2.2×10^{32} erg. The spin-down times associated with magnetic braking range between 39 and 78 Gyr. We also compute the emission measure from the (quiescent) closed corona and show that it remains approximately constant through these epochs at a value of $\sim 10^{50.6}\,cm^{-3}$. This suggests that a magnetic cycle of τ Boo may not be detected by X-ray observations. We further investigate the interaction between the stellar wind and the planet by estimating radio emission from the hot Jupiter that orbits at 0.0462 au from τ Boo. By adopting reasonable hypotheses, we show that, for a planet with a magnetic field similar to Jupiter (~ 14 G at the pole), the radio flux is estimated to be about 0.5–1 mJy, occurring at a frequency of 34 MHz. If the planet is less magnetized (field strengths roughly smaller than 4 G), detection of radio emission from the ground is unfeasible due to the Earth's ionospheric cut-off. According to our estimates, if the planet is more magnetized than that and provided the emission beam crosses the observer line-of-sight, detection of radio emission from τ Boo b is only possible by ground-based instruments with a noise level of $\lesssim 1$ mJy, operating at low frequencies.

Key words: MHD – methods: numerical – stars: individual: τ Bootis – stars: magnetic field – stars: winds, outflows – radio continuum: planetary systems.

1 INTRODUCTION

1.1 Magnetic cycles and stellar winds

τ Boo (spectral type F7V) is a remarkable object, not only because it hosts a giant planet orbiting very close to the star, but also because it is one of the few stars for which magnetic polarity reversals have been reported in the literature. So far, two polarity reversals

have been detected (Donati et al. 2008a; Fares et al. 2009), suggesting that it undergoes magnetic cycles similar to the Sun, but with a period that is about one order of magnitude smaller than the solar one. The polarity reversals in τ Boo seem to occur at a period of roughly 1 yr, switching from a negative poloidal field near the visible pole in 2006 June (Catala et al. 2007) to a positive poloidal field in 2007 June (Donati et al. 2008a), and then back again to a negative polarity in 2008 July (Fares et al. 2009). At these three observing epochs, τ Boo presented a dominant poloidal field, but in between the last observed reversal (more specifically, in 2008 January), the magnetic field of τ Boo switched to a predominantly

toroidal one. Subsequent observations confirm that τ Boo presents stable, periodic polarity reversals (Fares et al., in preparation), confirming the presence of a magnetic cycle with a duration of roughly 2 yr.

It is interesting to note that polarity reversals have been observed in other objects, but the confirmation of the presence of a cycle requires a long-term monitoring. Petit et al. (2009) observed the first polarity switch, mostly visible in the azimuthal component of the magnetic field, in the solar-mass star HD 190771. Later on, Morgenthaler et al. (2011) observed another polarity switch of HD 190771. Contrary to τ Boo, the initial magnetic state of this object was not recovered, suggesting that the polarity reversals in HD 190771 do not take the form of a solar-type cycle. Polarity reversals have also been reported in the other solar-type stars HD 78366 and ξ Boo A (Morgenthaler et al. 2011), while the young star HR 1817 showed an 'attempted' reversal in the azimuthal component of the magnetic field (Marsden et al. 2010). In this case, rather than undergoing a reversal, the magnetic field strength decreased, but then strengthened with the same polarity (Marsden et al. 2010).

The nature of such a short magnetic cycle in τ Boo remains an open question. Differential rotation is thought to play an important role in the solar cycle. The fact that τ Boo presents a much higher level of surface differential rotation than that of the Sun may be responsible for its short observed cycle.[1] In addition, τ Boo also hosts a close-in planet that, due to its close proximity to the star, may have been able to synchronize, through tidal interactions, the rotation of the shallow convective envelope of the host star with the planetary orbital motion. This presumed synchronization may enhance the shear at the tachocline, which may influence the magnetic cycle of the star (Fares et al. 2009).

As the stellar winds of cool stars are magnetic by nature, variations of the stellar magnetic field during the cycle directly influences the outflowing wind. The solar wind, for instance, is dominated by high-speed flows outflowing from the coronal holes during and near the minimum phases of the solar cycle. As the solar cycle approaches its maximum, the coronal holes become smaller and the high-speed flows narrow and weaken (Meyer-Vernet 2007). In analogy to the Sun, we expect that the stellar wind from τ Boo will respond to variations in the magnetic properties of the star during its cycle. One of the goals of this present study is to quantify these variations.

1.2 Radio emission from wind–planet interaction

The solar magnetic cycle has a direct impact on the planets of the Solar system. In particular at the Earth, during periods of intense solar activity, geomagnetic storms can, e.g., produce auroras, disrupt radio transmissions, affect power grids and damage satellites orbiting the Earth. Likewise, the magnetic cycle of τ Boo should affect any orbiting planet, especially if located at such a close distance as that of τ Boo b (0.0462 au $\simeq 6.8 R_\star$ from its host star; Butler et al. 1997).

In particular, the planet's interaction with the host star wind may lead to planetary radio emission. Radio emission has been detected in the giant planets of the Solar system, in the Earth and in a few satellites orbiting these planets (Zarka 1998). The auroral radio emission from the Earth, for instance, is pumped (primarily) by

reconnection events between the interplanetary magnetic field (embedded in the solar wind) and the planet's own magnetic field at the dayside magnetopause. On the other hand, the interaction of Jupiter with its moon Io, which also generates radio emission, is thought to be caused by the satellite's motion inside the planet's magnetosphere (Neubauer 1980).

Radio emission from exoplanets has been investigated by several authors (e.g. Bastian, Dulk & Leblanc 2000; Zarka et al. 2001; Lazio et al. 2004, 2010a,b; Grießmeier et al. 2005, 2007a; Stevens 2005; Grießmeier, Zarka & Spreeuw 2007b; Lazio & Farrell 2007; Zarka 2007; Jardine & Cameron 2008; Vidotto et al. 2010a; Nichols 2011; Vidotto, Jardine & Helling 2011b). Detection of the auroral radio signatures from exoplanets would consist of a direct planet-detection method, as opposed to the widely used indirect methods of radial velocity measurements or transit events. Moreover, the detection of exoplanetary radio emission would comprise a way to assess the magnitude of planetary magnetic fields.

However, despite many attempts, radio emission from exoplanets has not been detected so far. One of the reasons for the unsuccessful detection is attributed to the beamed nature of the electron–cyclotron maser instability, believed to be the process operating in the generation of radio emission. Poor instrumental sensitivity is also pointed to as an explanation for the lack of detection of radio emission from exoplanets. Another reason for the failure is often attributed to frequency mismatch: the emission process is thought to occur at cyclotron frequencies, which depend on the intensity of the planetary magnetic field. Therefore, planets with magnetic field strengths of e.g. a few G would emit at a frequency that could be either unobservable from the ground due to the Earth's ionospheric cut-off or that does not correspond to the operating frequencies of available instruments. In that regard, the low operating frequency of Low Frequency Array (LOFAR; current under commissioning), jointly with its high sensitivity at this low-frequency range, makes it an instrument that has the potential to detect radio emission from exoplanets. A more thorough discussion about the non-detection of radio emission from exoplanets can be found in e.g. Bastian et al. (2000) and Lazio et al. (2010b).

1.3 This work

To quantify the effect the stellar cycle has on the orbiting planet, one has to understand the properties of the stellar wind, which depend on the particular geometry of the coronal magnetic field at each epoch during the stellar cycle. Several works have studied the influence of the geometry of the coronal magnetic field on the stellar wind properties by means of numerical simulations (Keppens & Goedbloed 1999, 2000; Matt & Pudritz 2008; Vidotto et al. 2009a,b; 2010a, 2011a; Cohen et al. 2010; Pinto et al. 2011, among others). Here, we implement the observationally derived surface magnetic field of τ Boo in our numerical model. In total, we use in the present study four surface magnetic maps derived at four different epochs: 2006 June, 2007 June, 2008 January and 2008 July. These maps have been presented elsewhere (Catala et al. 2007; Donati et al. 2008a; Fares et al. 2009) and encompass (at least) one full cycle, with two polarity reversals in the poloidal field.

Using the results of our stellar wind models, we then evaluate the radio flux emitted by τ Boo b, analogously to what is observed for the giant planets in the Solar system. The radio emission is calculated at each observed epoch of the stellar magnetic cycle. We note that the τ Boo system has been classified among the prime targets for radio emission detection based on models that consider more simplistic descriptions for the stellar wind (e.g. Lazio

---

[1] Note however that, although also known to present high levels of differential rotation, HD 171488 seems not to have a fast magnetic cycle as the one reported for τ Boo (Marsden et al. 2006; Jeffers et al. 2011).

et al. 2004; Stevens 2005; Jardine & Cameron 2008; Reiners & Christensen 2010; Grießmeier et al. 2011). A more sophisticated model for the stellar wind, such as the one presented in this paper, will be useful to provide some interpretation of the radio emission when it is discovered.

This paper is organized as follows. Section 2 presents the three-dimensional numerical model used in our simulations and describes the observed surface magnetic field distributions that are implemented in our model. Section 3 presents the results of our stellar wind modelling, and in Section 4, we investigate planetary radio emission arising from the interaction between the stellar wind and the planet. Section 5 presents further discussion and the conclusions of our work.

2 STELLAR WIND MODEL

2.1 Numerical model

The lack of symmetry in the magnetic field distribution at the surface of τ Boo requires the stellar wind equations to be solved in a fully three-dimensional geometry. Our simulations make use of the three-dimensional magnetohydrodynamics (MHD) numerical code BATS-R-US developed at University of Michigan (Powell et al. 1999). BATS-R-US has been widely used to simulate e.g. the Earth's magnetosphere (Ridley et al. 2006), the heliosphere (Roussev et al. 2003), the outer heliosphere (Linde et al. 1998; Opher et al. 2003, 2004), coronal mass ejections (Manchester et al. 2004; Lugaz, Manchester & Gombosi 2005) and the magnetosphere of planets (Tóth et al. 2004; Hansen et al. 2005), among others. It solves the ideal MHD equations that in the conservative form are given by

$$\frac{\partial \rho}{\partial t} + \nabla \cdot (\rho \boldsymbol{u}) = 0, \tag{1}$$

$$\frac{\partial (\rho \boldsymbol{u})}{\partial t} + \nabla \cdot \left[\rho \boldsymbol{u} \boldsymbol{u} + \left(p + \frac{B^2}{8\pi} \right) I - \frac{\boldsymbol{B} \boldsymbol{B}}{4\pi} \right] = \rho \boldsymbol{g}, \tag{2}$$

$$\frac{\partial \boldsymbol{B}}{\partial t} + \nabla \cdot (\boldsymbol{u} \boldsymbol{B} - \boldsymbol{B} \boldsymbol{u}) = 0, \tag{3}$$

$$\frac{\partial \varepsilon}{\partial t} + \nabla \cdot \left[\boldsymbol{u} \left(\varepsilon + p + \frac{B^2}{8\pi} \right) - \frac{(\boldsymbol{u} \cdot \boldsymbol{B}) \boldsymbol{B}}{4\pi} \right] = \rho \boldsymbol{g} \cdot \boldsymbol{u}, \tag{4}$$

where the eight primary variables are the mass density ρ, the plasma velocity $\boldsymbol{u} = \{u_r, u_\theta, u_\varphi\}$, the magnetic field $\boldsymbol{B} = \{B_r, B_\theta, B_\varphi\}$ and the gas pressure p. The gravitational acceleration due to the star with mass $M_\star$ and radius $R_\star$ is given by $\boldsymbol{g}$, and ε is the total energy density given by

$$\varepsilon = \frac{\rho u^2}{2} + \frac{p}{\gamma - 1} + \frac{B^2}{8\pi}. \tag{5}$$

We consider an ideal gas, so $p = nk_B T$, where k_B is the Boltzmann constant, T is the temperature, $n = \rho/(\mu m_p)$ is the particle number density of the stellar wind, μm_p is the mean mass of the particle and γ is the polytropic index (such that $p \propto \rho^\gamma$).

At the initial state of the simulations, we assume that the wind is thermally driven (Parker 1958). At the base of the corona ($r = R_\star$), we adopt a wind coronal temperature T_0, wind number density n_0 and stellar rotation period P_{rot}. The values adopted in our simulations are shown in Table 1. The values of $M_\star$ and $R_\star$ are from Takeda et al. (2007) and P_{rot} from Fares et al. (2009). The value of T_0 we adopted represents a typical temperature of a stellar corona and n_0 is selected in such a way as to recover observed emission

Table 1. Adopted parameters for the simulations.

	Parameter	Value
Stellar mass	$M_\star (\mathrm{M}_\odot)$	1.341
Stellar radius	$R_\star (\mathrm{R}_\odot)$	1.46
Stellar rotation period	P_{rot} (d)	3.0
Coronal base temperature	T_0 (MK)	2
Coronal base density	n_0 (cm^{-3})	10^9
Polytropic index	γ	1.1
Particle mean mass	$\mu (m_p)$	0.5

measure (EM) values (see Section 3). With this numerical setting, the initial solution for the density, pressure (or temperature) and wind velocity profiles is fully specified.

To complete our initial numerical set-up, we assume that the magnetic field is potential everywhere (i.e. $\nabla \times \boldsymbol{B} = 0$). To provide an initial solution for $\boldsymbol{B}$, we use the potential field source surface method (PFSSM; Altschuler & Newkirk 1969; Jardine, Collier Cameron & Donati 2002), which assumes that beyond a given radius (which defines a spherical *source surface*), the magnetic field lines are purely radial. The initial solution for $\boldsymbol{B}$ is found once the radial component of the magnetic field B_r at the surface of the star is specified and a distance to the source surface is assumed (set at $4R_\star$ in the initial state of our runs). In our simulations, we incorporate B_r derived from the observations, similarly to the method presented in Vidotto et al. (2011a). Section 2.2 presents the surface magnetic field maps used in this study.

Once set at the initial state of the simulation, the distribution of B_r is held fixed at the surface of the star throughout the simulation run, as are the coronal base density and thermal pressure. A zero radial gradient is set to the remaining components of $\boldsymbol{B}$ and $\boldsymbol{u} = 0$ in the frame corotating with the star. The outer boundaries at the edges of the grid have outflow conditions, i.e. a zero gradient is set to all the primary variables. The rotation axis of the star is aligned with the z-axis, and the star is assumed to rotate as a solid body.

Our grid is Cartesian and extends in x, y and z from -20 to $20R_\star$, with the star placed at the origin of the grid. BATS-R-US uses block adaptive mesh refinement (AMR), which allows for variation in numerical resolution within the computational domain. The finest resolved cells are located close to the star (for $r \lesssim 4R_\star$), where the linear size of the cubic cell is $0.039R_\star$. The coarsest cell is about one order of magnitude larger (linear size of $0.31R_\star$) and is located at the outer edges of the grid. The total number of cells in our simulations is about 6.5 million.

As the simulations evolve in time, both the wind and magnetic field lines are allowed to interact with each other. The resultant solution, obtained self-consistently, is found when the system reaches steady state (in the reference frame corotating with the star). Our simulations run for two to three stellar rotations periods (6–9 d of physical time). Despite the initial assumption of a potential field, we remind the reader that the steady-state solution, shown in the remainder of this paper, deviates from a potential solution and currents are created in the system (see Appendix A for a comparison between both solutions). Likewise, the initially spherically symmetric hydrodynamical quantities (ρ, p, $\boldsymbol{u}$) evolve to asymmetric distributions.

2.2 Adopted surface magnetic field distributions

The surface magnetic maps used in this study were reconstructed using Zeeman–Doppler imaging (ZDI), a tomographic imaging
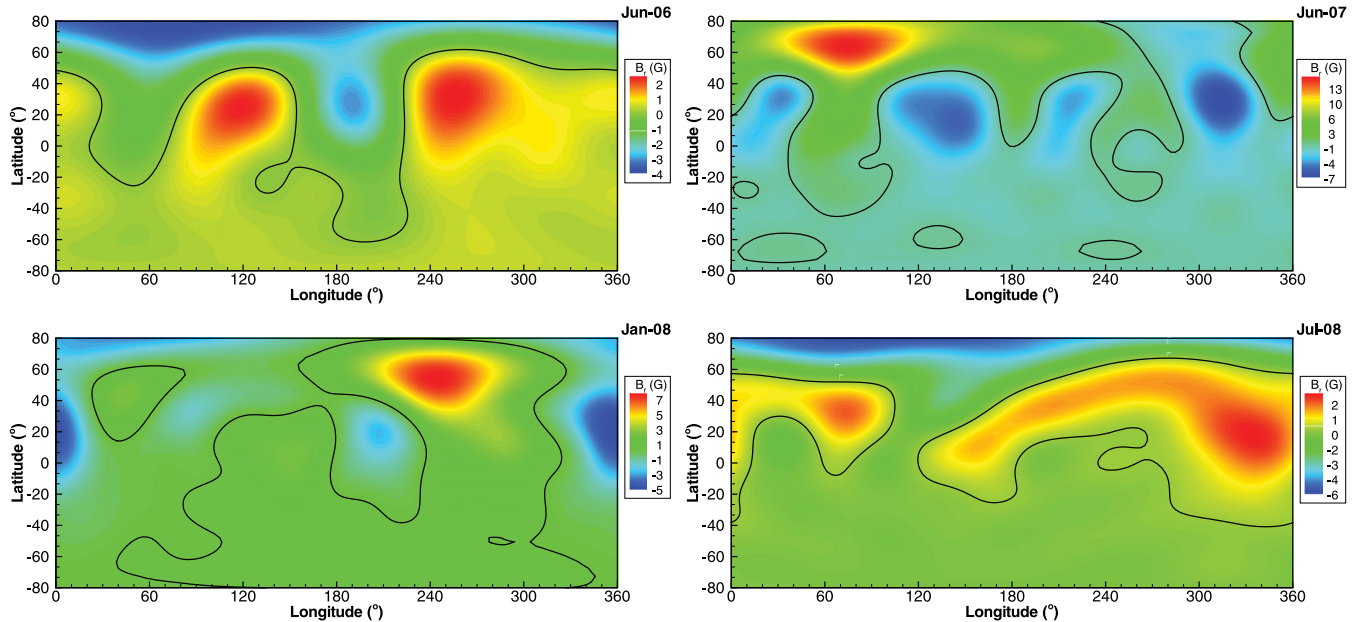
Figure 1. Surface distribution of the radial component of the magnetic field of τ Boo reconstructed from observations using ZDI (Catala et al. 2007; Donati et al. 2008a; Fares et al. 2009). The black solid lines represent $B_r = 0$ G.
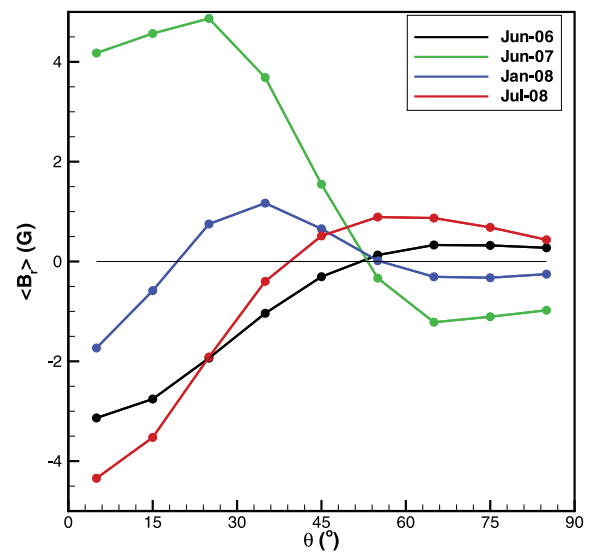
Table 2. Main properties of the observed surface magnetic field. The polarity of the poloidal component is described around the visible rotation pole and the phase of the cycle is calculated assuming a cycle period of $P_{cyc} = 800$ d. The unsigned surface magnetic flux in the radial component is Π_0.

Date	Cycle phase	Dominant component	Polarity	Π_0 (10^{22} Mx)
2006 June	0.12	Poloidal	Negative	11.4
2007 June	0.58	Poloidal	Positive	23.5
2008 January	0.86	Toroidal	Mixed	14.0
2008 July	0.07	Poloidal	Negative	12.1

Figure 2. Average intensity of B_r calculated at bins of colatitude θ. Along with Table 2 and Fig. 1, it shows the similarities between the maps obtained in 2006 June (black solid line) and 2008 July (red solid line).

technique (e.g. Donati & Brown 1997). Using ZDI, one can reconstruct the large-scale magnetic field (intensity and orientation) at the surface of the star from a series of circular polarization spectra. The radial component of the reconstructed surface magnetic maps is shown in Fig. 1 for the four different epochs considered here: 2006 June (Catala et al. 2007), 2007 June (Donati et al. 2008a), 2008 January and 2008 July (Fares et al. 2009).

Table 2 presents a summary of the main properties of the observed large-scale magnetic field distributions. The unsigned surface magnetic flux is calculated over the surface of the star ($S_\star$) as $\Pi_0 = \oint |B_r(R_\star)| dS_\star$. Fig. 2 shows the average value of the radial component calculated over colatitude bins of $10°$. From Table 2 and Figs 1 and 2, we note that the magnetic field distribution in 2008 July shows similarities to the one in 2006 June, suggesting that the magnetic state of 2006 June seems to be recovered in 2008 July. Fares et al. (2009) found a preferred cycle period of about $P_{cyc} = 800$ d, although a much shorter period of 250 d was not excluded. For $P_{cyc} = 800$ d, the maps derived in 2006 June and 2008 July should describe similar phases at two consecutive cycles.

We note that, due to the lack of information in the unseen hemisphere of the star (latitudes $\lesssim -40°$), the reconstructed magnetic field there has essentially no energy (unconstrained field reconstruction). However, constraints on the property of the magnetic field in the unseen hemisphere could have been imposed (e.g. see Lang et al. 2012). These constraints are adopted based on physical properties of the star. For example, for the classical T Tauri star BP Tau, antisymmetric field configurations (with respect to the centre of the star) are preferred as they are the only ones capable of yielding the high-latitude anchoring of accretion funnels (Donati et al. 2008b). Without a physical reason to justify the choice of a symmetric/antisymmetric topology, we adopt in this work the unconstrained maps. In Appendix B, we show that different assumptions adopted during the field reconstruction in the unseen hemisphere of the star (latitudes $\lesssim -40°$) do not have an appreciable effect on the results presented in this paper.
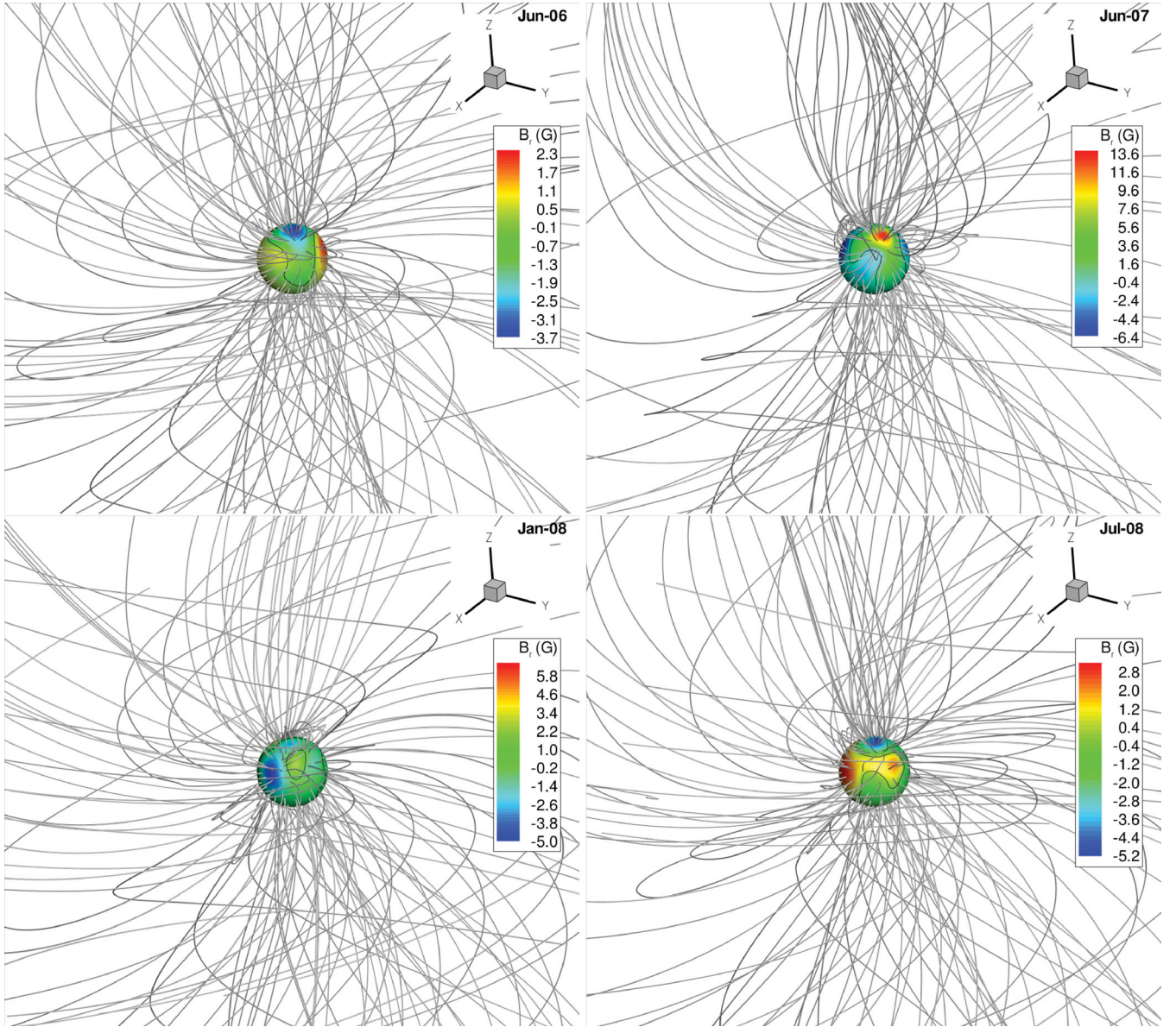
Figure 3. Three-dimensional view of the final configuration of the magnetic field lines (grey lines) of the corona of τ Boo for the four cases analysed in this paper. The radial magnetic field is shown at the surface of the star in colour-scale. The rotational axis of the star is along the *z*-axis, the equator is in the *xy*-plane.

3 RESULTS: STELLAR WIND PROPERTIES

The properties of the stellar wind depend on the particular geometry of the coronal magnetic field, which varies through the stellar cycle. Ideally, if one wishes to investigate the smooth evolution of the stellar wind through the cycle, the evolution of the large-scale magnetic field at the base of the corona should be incorporated in the simulations by means of a time-dependent boundary condition for B. To do that, one needs surface magnetic distributions that are reasonably well time-sampled throughout the cycle.

In the present study, we make use of four available surface magnetic maps that were obtained at intervals of 6 months to 1 yr. Therefore, the wind solutions found for each of these observing epochs represent a *snapshot* of the stellar wind at each given epoch. Implicitly, we are assuming that the time for the wind to adjust to the evolution of the surface magnetic field occurs in a faster time-scale than the dynamical time-scale of the magnetic evolution. This

sounds a reasonable hypothesis, as in our simulations, for a typical wind velocity of about $300 \, \text{km s}^{-1}$, a spatial scale of $20R_\star$ (half-size of our grid) will be covered in less than a day, while, due to high surface differential rotation, it is likely that significant magnetic field evolution should occur on a longer time-scale of a few weeks.[2]

Fig. 3 shows the final configuration of the magnetic field lines in the corona of τ Boo for different epochs. We note that, due to the presence of the wind, the magnetic field lines become twisted around the rotation axis (*z*-axis). The wind velocity in the equatorial plane of the star (*xy*-plane) is shown in Fig. 4. We note that both the coronal magnetic field lines and the wind velocity profile vary through the cycle.

---

[2] For a latitude rotational shear of $d\Omega = 0.46 \, \text{rad d}^{-1}$ (Fares et al. 2009), the time for the equator to lap the pole by one complete rotation cycle is about 2 weeks.
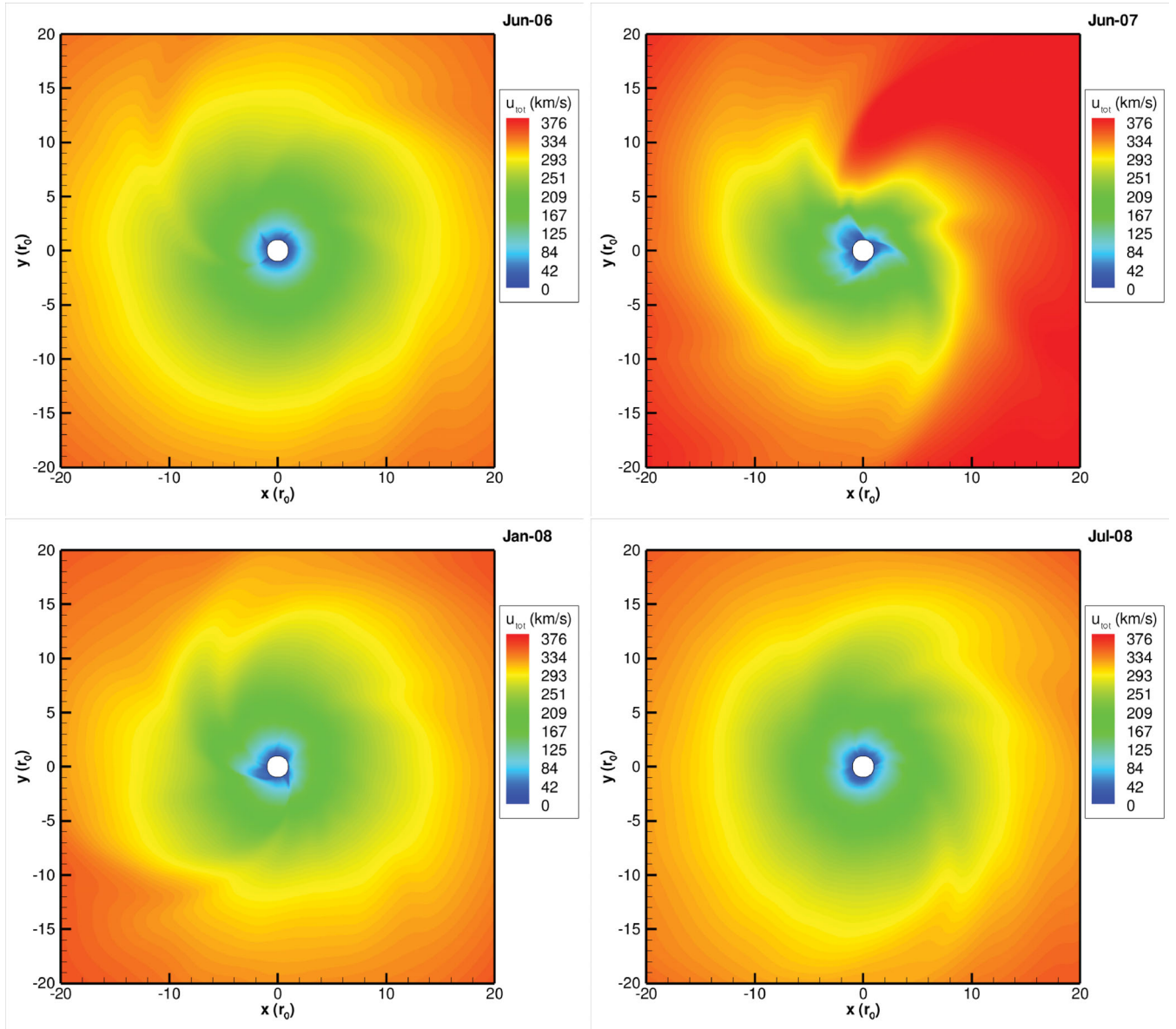
Figure 4. The wind velocity distributions for each epoch are shown in the equatorial plane of the star.

For each epoch, we compute the mass-loss rate, defined as the flux of particles flowing across a closed surface S:

$$\dot{M} = \oint_S \rho \boldsymbol{u} \cdot \mathrm{d}\boldsymbol{S}. \tag{6}$$

The calculated $\dot{M}$ for each cycle phase is presented in Table 3, where we note that the derived mass-loss rates are about two orders of magnitude larger than the solar wind value ($\dot{M}_\odot \sim 2 \times 10^{-14}\,\mathrm{M}_\odot\,\mathrm{yr}^{-1}$). We warn the reader that the values of $\dot{M}$ obtained here (and, in general, by any stellar wind models) strongly depend on the choice of the base density n_0. One way to constrain coronal base densities is to perform a direct comparison between our derived mass-loss rates and the observationally determined ones. However, to the best of our knowledge, mass-loss rates determination for τ Boo are not available in the literature. A less-direct way to constrain coronal base densities is through the comparison of EM values derived from X-ray spectra. Coronal X-ray emission comes from flaring loops with different sizes. The net effect of the superposition of the small-scale loops should be to form the observed regions of closed magnetic field lines (large-scale structure). Therefore, to compute the EM, we concentrate only on the closed field line regions. The EM is defined as

$$\mathrm{EM} = \int n_e n_i \, \mathrm{d}V_{\mathrm{closed}} = \int n_e^2 \, \mathrm{d}V_{\mathrm{closed}}, \tag{7}$$

where n_e and n_i are the electron and ion number densities, respectively. The integration above is performed in the region of closed field lines (with a volume V_{closed}), where the temperature is ~ 1.5–2×10^6 K. The values obtained are presented in Table 3. We found that EM $\sim 10^{50.6}\,\mathrm{cm}^{-3}$, which is consistent with observations of Maggio, Sanz-Forcada & Scelsi (2011), who found that the EM distribution peaks at $\sim 10^{51}\,\mathrm{cm}^{-3}$. This suggests that our choice for the coronal base density is representative of τ Boo, implicating that this star might indeed have a denser wind than that of the Sun ($\dot{M} \approx 135\,\dot{M}_\odot$ according to our models).

Table 3. Summary of the results of the simulations. The columns are, respectively, the date of the observations from which the surface magnetic maps were derived (Fig. 1), the mass-loss rate ($\dot{M}$), EM computed in the closed field line region, angular-momentum-loss rate ($\dot{J}$), spin-down time (τ), unsigned open magnetic flux (Π_{open}) and the ratio of the unsigned open magnetic flux to unsigned surface flux ($f_{\mathrm{open}} = \Pi_{\mathrm{open}}/\Pi_0$).

Date	$\dot{M}$ $(10^{-12}\,\mathrm{M_\odot\,yr^{-1}})$	EM $(10^{50}\,\mathrm{cm^{-3}})$	$\dot{J}$ $(10^{32}\,\mathrm{erg})$	τ (Gyr)	Π_{open} $(10^{22}\,\mathrm{Mx})$	f_{open}
2006 June	2.67	4.4	1.2	71	9.5	0.84
2007 June	2.75	4.3	2.2	39	20.5	0.87
2008 January	2.69	4.3	1.4	61	11.2	0.80
2008 July	2.68	4.4	1.1	78	9.0	0.74

Higher $\dot{M}$ are also predicted/estimated by other authors. In a recent paper, Cranmer & Saar (2011) developed a model that predicts mass-loss rates of cools stars directly from stellar parameters. As τ Boo is within the range covered by the Cranmer & Saar scaling, we used their provided IDL routine to compute $\dot{M}$ predicted by their models. Using the stellar parameters shown in Table 1, the metallicity ([Fe/H] = 0.23) and stellar luminosity ($\log(L_\star/\mathrm{L_\odot}) = 0.481$) provided by Valenti & Fischer (2005), the scaling relations developed by Cranmer & Saar (2011) predict that τ Boo should have $\dot{M} \approx 330\,\dot{\mathrm{M}}_\odot \approx 6.6 \times 10^{-12}\,\mathrm{M_\odot\,yr^{-1}}$. Other estimates were derived by Stevens (2005, $\dot{M} \approx 83.4\,\dot{\mathrm{M}}_\odot \approx 1.67 \times 10^{-12}\,\mathrm{M_\odot\,yr^{-1}}$) and Reiners & Christensen (2010, $\dot{M} \approx 198.5\,\dot{\mathrm{M}}_\odot \approx 3.97 \times 10^{-12}\,\mathrm{M_\odot\,yr^{-1}}$), who adopted the empirically derived relation between $\dot{M}$ and the X-ray flux from Wood et al. (2002, 2005). These predictions/estimates are consistent with our results, namely that the wind mass-loss rate of τ Boo should be significantly higher than the solar value.

The wind outflowing along magnetic field lines carries away stellar angular momentum, therefore, exerting a braking torque in the star. However, it is known that F-type stars are not very efficient in losing angular momentum. This can be seen, for instance, in the open cluster NGC 6811 which, at an age of 1 Gyr (Meibom et al. 2011), still presents F-type stars that are rapidly rotating, while redder stars (main-sequence G stars) have spun down more considerably. To examine the stellar magnetic braking, we evaluate the angular-momentum-loss rate carried by the wind of τ Boo as (Mestel & Selley 1970)

$$\dot{J} = \oint_{S_A} \left(p + \frac{B^2}{8\pi} \right) (r \times \hat{n})_z + \rho V \cdot \hat{n}\, [r \times (\Omega \times r)]_z \, \mathrm{d}S_A, \quad (8)$$

where $V = u - \Omega \times r$ is the velocity vector in the frame rotating with angular velocity Ω, S_A is the Alfvén surface and $\hat{n}$ is the normal unit vector to the Alfvén surface. We obtained that $\dot{J}$ varies during the observed phases of the cycle, ranging from 1.1 to 2.2×10^{32} erg (Table 3).

We also estimate the time-scale for rotational braking as $\tau = J/\dot{J}$, where J is the angular momentum of the star. If we assume a spherical star with a uniform density, then $J = 0.4 M_* R_*^2 \Omega_*$ and the time-scale is

$$\tau \simeq \frac{9 \times 10^{33}}{\dot{J}} \left(\frac{M_*}{\mathrm{M_\odot}} \right) \left(\frac{1\,\mathrm{d}}{P_{\mathrm{rot}}} \right) \left(\frac{R_*}{\mathrm{R_\odot}} \right)^2 \, \mathrm{Gyr} \quad (9)$$

(Vidotto et al. 2011a). Our results are also shown in Table 3. For τ Boo, spin-down times (spanning from 39 to 78 Gyr) are an order of magnitude larger than its age (about 2.4 Gyr; Saffe, Gómez & Chavero 2005), suggesting that, if the stellar wind is the only contributor of redistribution of angular momentum of the star, τ Boo should maintain its relatively high rotation rate during its main-sequence lifetime.

The reconstructed maps used here do not have error bars. Therefore, we cannot assess the error that is propagated in our simulations due to associated uncertainties from the observations. We evaluate the accuracy in our simulations by calculating the largest variations found across the simulation domain (essentially due to changes in grid resolution). The accuracy varies between cases; in the worst scenario, an accuracy of 1.2 per cent is found for $\dot{M}$ and of 16 per cent for $\dot{J}$.

Table 3 also shows the amount of (unsigned) flux in the open magnetic field lines,

$$\Pi_{\mathrm{open}} = \oint_S |B_r|\, \mathrm{d}S, \quad (10)$$

along which the stellar wind is channelled. Note that the integral in equation (10) is performed over a spherical surface S. The open flux is calculated sufficiently far from the star ($\gtrsim 10 R_\star$). The fraction of open flux, defined as $f_{\mathrm{open}} = \Pi_{\mathrm{open}}/\Pi_0$, is also presented in Table 3.

A closer inspection of Table 3 shows that for τ Boo, mass-loss rates do not vary significantly during the observed epochs of the stellar cycle (variation is at most 3 per cent), while the angular-momentum-loss rate varies by a factor of about 2. Similarly to the mass-loss rates, the EM shows a negligible variation during the observed epochs of the cycle ($\lesssim 3$ per cent).

The fact that τ Boo's calculated EM does not vary during the cycle suggests that this star should not present significant variations in its quiescent X-ray emission during its cycle and a magnetic cycle of τ Boo may not be detected by X-ray observations. Indeed, a recent work points in this direction (Poppenhaeger, Günther & Schmitt 2012).

As already mentioned in Section 2.2, given the similarities of the surface magnetic distributions of τ Boo derived in 2006 June and 2008 July, these maps appear to describe similar cycle phases at distinct magnetic cycles. Because the properties of the stellar wind depend on the particular characteristic of the magnetic field, we expect the stellar wind at these two distinct epochs to be similar. As can be seen in Table 3, this is indeed what is found.

To investigate the variation during the cycle, we present in Fig. 5 sinusoidal fits to both the observed data (Fig. 5a) and the results of the wind modelling shown in Table 3 (Figs 5b–d). For comparison purposes, using the two cycle periods obtained by Fares et al. (2009), two fits were done for each panel: the black line adopts a cycle period of 800 d, while the red line one of 250 d. Fig. 5(a), which shows the variation of the unsigned observed surface flux, illustrates the cyclic nature of the large-scale magnetic field of τ Boo. The same behaviour is seen in the plot of the open magnetic flux (Fig. 5b). The remaining panels of Fig. 5 illustrate the evolution of $\dot{M}$ and $\dot{J}$ through the stellar magnetic cycle, showing that the stellar wind also behaves in a cyclic way. Note however the very small amplitudes in the variation of $\dot{M}$.
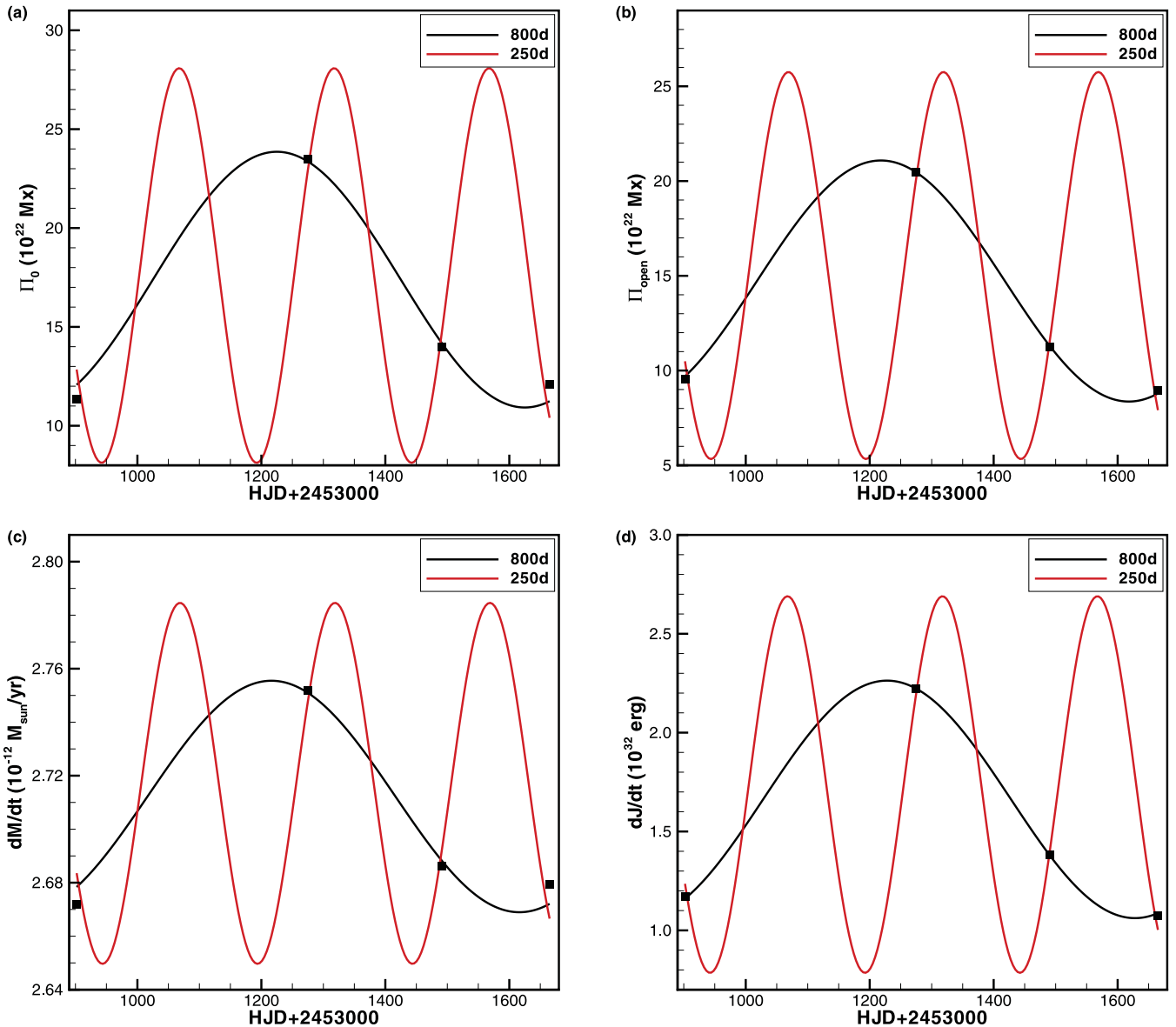
Figure 5. Temporal evolution of selected quantities evaluated at four different epochs of the stellar magnetic cycle (black squares, see Table 3). Sinusoidal fits to these quantities are shown for a cycle period of 800 d (black solid line) and for 250 d (red solid line). The quantities shown are (a) unsigned surface flux, (b) unsigned open flux, (c) mass-loss rates and (d) angular-momentum-loss rates.

4 RESULTS: RADIO EMISSION FROM WIND–PLANET INTERACTION

In this section, we present an estimate of radio flux that should arise from the interaction of τ Boo b's magnetic field with the stellar wind. For that, we use the results of our models, presented in Section 3. We note that the lack of knowledge of some properties of the planet, such as its radius or its magnetic field intensity, leads us to adopt some (reasonable) hypotheses. These hypotheses are clearly stated in the following paragraphs. Section 5 presents a discussion about how different assumptions would change our results.

The first unknown quantity in our calculations is the orbital inclination of τ Boo b. The position of the planet is required because the characteristics of the host star wind are three-dimensional in nature. Therefore, the characteristics of the ambient medium surrounding

the planet, with which the planet will inevitably interact, depend on the planet's position (orbital distance, longitude and colatitude). It is worth mentioning that, because of the large differential rotation of τ Boo (the equator rotates with a period of 3 d, while near the poles at 3.9 d), at the colatitude of $\sim$45°, the planetary orbital period and the stellar surface rotation are similar. The orbital ephemeris used in the stellar surface magnetic maps of Catala et al. (2007), Donati et al. (2008a) and Fares et al. (2009) places the conjunction of the planet at the stellar rotation phase 0.0, which constrain the meridional plane where the planet should be located: in the configuration shown in Fig. 3, this is at the xz-plane (more precisely in the region of $x < 0$). The orbital radius of the planet has been determined to be 0.0462 au (Butler et al. 1997), which is about $6.8R_\star$. The orbital inclination of the planet, if known, would constrain at which colatitude the planet is orbiting. Because of this unknown, the next
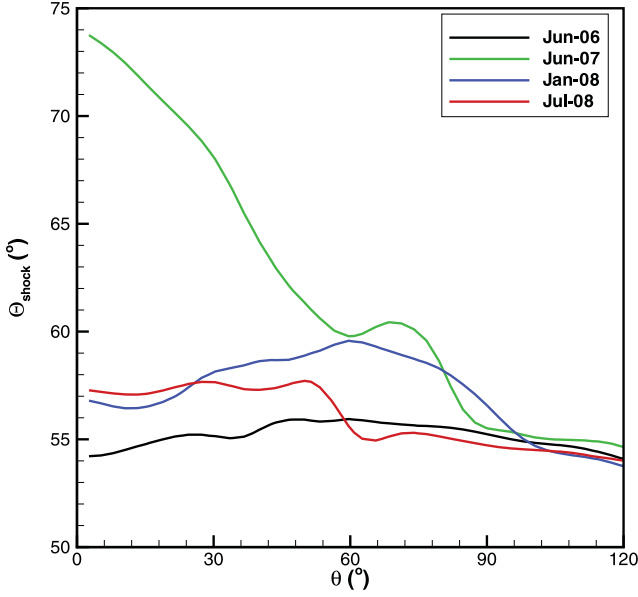
Figure 6. Variation of the shock angle Θ_{shock} for the observed epochs of the stellar cycle as a function of colatitude θ of the planet orbit.

calculations are computed for a range of colatitudes θ, where $\theta = 0°$ is at the rotation pole of the star (in the visible hemisphere) and $\theta = 90°$, the equatorial plane of the star.

As the planet orbits around its host star, it interacts with the stellar wind, which, in the case of τ Boo, varies during the stellar magnetic cycle, as a response to variations in the stellar magnetic field (Section 3). At the orbital distance of τ Boo b, the interaction between the planet and the stellar wind takes place at supermagnetosonic velocities, ensuing the formation of a bow-shock around the planet. We define the angle Θ_{shock} that the shock normal makes to the relative azimuthal velocity of the planet as

$$\Theta_{\text{shock}} = \arctan\left(\frac{u_r}{v_K - u_\varphi}\right), \tag{11}$$

where we assume the planet to be at a circular Keplerian orbit ($v_K = (GM_\star/r_{\text{orb}})^{1/2}$). When the shock normal points to the host star, $\Theta_{\text{shock}} = 90°$ and the shock is a dayside shock (Vidotto, Jardine & Helling 2010b), similar to the one that surrounds the Earth's magnetosphere (Schwartz 1998). On the other hand, for a shock normal pointing ahead of the planetary orbit, $\Theta_{\text{shock}} = 0°$ and the shock is an ahead shock (Vidotto et al. 2010b). Fig. 6 shows how the angle Θ_{shock} varies through the observed phases of the stellar cycle for a range of colatitudes θ. We see that the shock formed around τ Boo b's magnetosphere forms at angles $52° \lesssim \Theta_{\text{shock}} \lesssim 74°$.

The magnetosphere of the planet deflects the stellar wind around it, forming a cavity in the wind. The extent of the planetary magnetosphere r_M can be determined by static pressure balance (e.g. Vidotto et al. 2011b):

$$\rho \Delta u^2 + \frac{B^2}{8\pi} + p = \frac{B_p^2(r_M)}{8\pi} + p_p, \tag{12}$$

where $|\Delta \boldsymbol{u}| = |\boldsymbol{u} - \boldsymbol{v}_K|$ is the relative velocity between the wind and the planet, and ρ, p and B are the local density, pressure and magnetic field intensity at the ambient medium surrounding the planet. $B_p(r_M)$ is the intensity of the planet's magnetic field at the nose of the magnetopause. In equation (12), we neglect compression of the planetary magnetic field (pile-up). In our next calculations, we neglect the planet thermal pressure p_p. We assume that the planetary magnetic field is dipolar, such that $B_p(r_M) = B_{p,\text{eq}}(R_p/R)^3$, where

R_p is the planetary radius, R is the radial coordinate centred at the planet, $B_{p,\text{eq}} = B_p/2$ is the magnetic field intensity evaluated at the equator of the planet and B_p at its pole. Assuming the dipole is aligned with the planetary orbital spin axis, the magnetospheric radius (i.e. where $R = r_M$) is given by

$$\frac{r_M}{R_p} = \left[\frac{(B_p/2)^2}{8\pi(\rho \Delta u^2 + p) + B^2}\right]^{1/6}. \tag{13}$$

Fig. 7(a) shows how the magnetospheric radius of τ Boo b varies through the observed epochs of the stellar magnetic cycle. The magnetic field of the planet is a quantity that has not yet been directly observed for extrasolar planets. If confirmed, the technique proposed by Vidotto et al. (2010b), based on near-ultraviolet (UV) transit observations, should provide a useful tool in determining planetary magnetic field intensities for transiting systems. In their estimates for WASP-12b (the only case for which near-UV data are available so far), they placed an upper limit on the intensity of the planetary magnetic field of about the same order of magnitude as Jupiter's magnetic field. Dynamo models of Sánchez-Lavega (2004) suggest that close-in giant planets should present a magnetic field intensity similar to the Earth's. To accommodate these two suggestions, we assume the planet to have a magnetic field intensity similar to that of the Earth ($B_p = 1$ G, right axis in Fig. 7a) and Jupiter ($B_p = 14$ G, left axis). For a terrestrial magnetic field intensity, the planet's magnetospheric size is quite small ($1.36 < r_M/R_p < 1.46$), while it is a few times larger for a Jovian magnetic field intensity ($3.2 < r_M/R_p < 3.6$). Because the characteristics of the stellar wind is the same for both cases (left-hand side of equation 12), the smallest magnetospheric radius for the case with $B_p = 1$ G is due to the smallest magnetic moment assumed. We note that the former case is quite similar to the size of the magnetosphere of Mercury (~ 1.3–1.9 Mercury radii; Russell, Baker & Slavin 1988). For comparison, the radius of the Earth's magnetosphere is ~ 10–15 $R_\oplus$ (Shue & Song 2002). Furthermore, we note that the magnetospheric size variations through the cycle are at most of ~ 5 per cent depending on the colatitude θ (related to the orbital inclination).

In the Solar system, the planetary radio power P_{radio} is related to the impacting solar wind kinetic and magnetic powers (P_k and P_B, respectively). Kinetic-to-radio efficiency is $P_k/P_{\text{radio}} = 10^{-5}$, and magnetic-to-radio efficiency is $P_B/P_{\text{radio}} = 2 \times 10^{-3}$ (Zarka 2007). We assume that the same efficiency ratios will hold in the τ Boo planetary system.

The kinetic power of the impacting wind on the planet is approximated as the ram pressure of the wind ($\rho(\Delta u)^2$) impacting in the planet, whose area is πr_M^2, at a (relative) velocity Δu:

$$P_k \simeq \rho(\Delta u)^3 \pi r_M^2. \tag{14}$$

By using the results of our simulations in the previous equation, we are thus able to compute the impacting kinetic power of the wind. Note that our models can only obtain the magnetospheric size of the planet relative to its radius (Fig. 7a). To convert the relative magnetospheric size to a physical value we need information on the unknown radius of the planet R_p (note that τ Boo b is not transiting its host star). Following Sánchez-Lavega (2004) and Grießmeier et al. (2007a), we adopt $R_p = 1.3 R_{\text{jup}}$. Fig. 7(b) shows how P_k varies through the observed epochs of the stellar magnetic cycle. With the assumed kinetic-to-radio efficiency as that observed for the Solar system planets ($P_{\text{radio}} \sim 10^{-5} P_k$), we conclude that radio power emitted by τ Boo b should be $P_{\text{radio}} \simeq 0.7$–$1.9 \times 10^{14}$ W for $B_p = 14$ G and $P_{\text{radio}} \simeq 0.12$–$0.33 \times 10^{14}$ W for $B_p = 1$ G.

Because the frequency of the radio emission is related to the cyclotron frequency, the magnitude of the planet's magnetic field
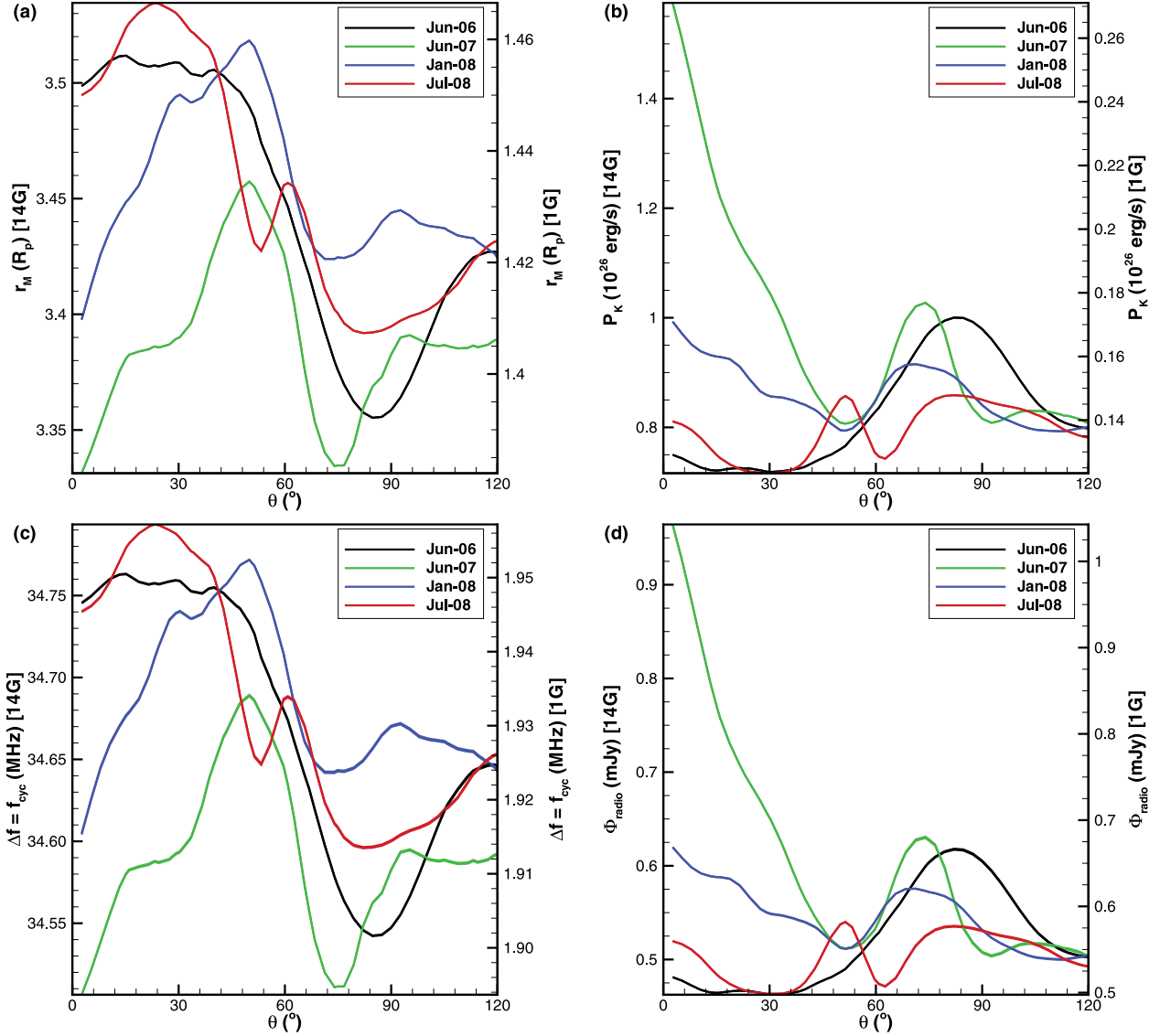
Figure 7. (a) Magnetospheric radius of τ Boo b as a function of colatitude θ, which is related to the planet's unknown orbital inclination (see text). The planet is either assumed to have a magnetic field intensity similar to the Earth (right axis) or similar to Jupiter's (left axis). (b) Wind kinetic power impacting in the planet. (c) Frequency of the radio emission. (d) Radio flux estimated for τ Boo b.

is required to estimate the bandwidth Δf of the radio emission. In Jupiter, decametric emission is thought to arise in a ring surrounding the auroral region wherein the planetary magnetic field lines are open. The aperture of the auroral ring can be related to the size of the planet's magnetosphere r_M as

$$\alpha_0 = \arcsin\left[\left(\frac{R_p}{r_M}\right)^{1/2}\right], \tag{15}$$

where α_0 is the colatitude of this auroral ring (more details in Vidotto et al. 2011b). The planetary magnetic field at colatitude α_0 is

$$B(\alpha_0) = \frac{B_p}{2}\left(1 + 3\cos^2\alpha_0\right)^{1/2}. \tag{16}$$

We assume that the emission bandwidth Δf is approximately the cyclotron frequency (Grießmeier et al. 2007a), where

$$\Delta f = f_{cyc} = 2.8\left(\frac{B(\alpha_0)}{1\,G}\right)\,MHz. \tag{17}$$

Fig. 7(c) shows the predicted emission bandwidth from τ Boo b assuming $B_p = 14\,G$ ($\Delta f \simeq 34\,MHz$) and assuming $B_p = 1\,G$ ($\Delta f \simeq 2\,MHz$). As the ionospheric cut-off is at frequencies $\lesssim 10\,MHz$, we note that if τ Boo b has a magnetic field similar to that of the Earth, we would not be able to detect any planetary emission from the ground. Using equation (17), we roughly estimate the minimum planetary magnetic field intensity required for the radio frequency to lie above the cut-off value of 10 MHz to be $B_{min} \sim 4\,G$. We note that, for $B_p = 14\,G$, the predicted $\Delta f \simeq 34\,MHz$ lies in the observable range of LOFAR.

The radio flux is related to the radio power as

$$\phi_{radio} = \frac{P_{radio}}{d^2\omega\Delta f}, \tag{18}$$

where $d = 15.6\,pc$ is the distance to the system and $\omega = 2 \times 2\pi(1 - \cos\alpha_0)$ is the solid angle of the emission (the factor of 2 was included in order to account for emission coming from both

northern and southern auroral rings). The radio flux is presented in Fig. 7(d) which shows that $\phi_{radio} \simeq 0.5$–1 mJy.[3]

There are in the literature some estimates of radio emission from τ Boo b. In the most optimistic consideration made by Farrell, Desch & Zarka (1999), the median radio flux of τ Boo b is estimated to be about 2.2 mJy, at a frequency of 28 MHz. Grießmeier et al. (2005) suggest a radio flux of 4–9 mJy at a frequency of 7–19 MHz. Although their assumptions for the stellar wind differ from our adopted model, the results obtained here are comparable to those from Farrell et al. (1999) and Grießmeier et al. (2005).

Lazio & Farrell (2007) observed τ Boo with the Very Large Array (VLA) at a frequency of 74 MHz (4-m wavelength). Observations were held at four epochs and radio emission was not detected at any of these epochs above a limit of about 100–300 mJy. The estimates presented here are in accordance to these observational findings as, indeed, our estimates predict an order of magnitude smaller flux at a different frequency.

We note that, for a radio emission process that is powered by reconnection events between the planetary magnetic field and the stellar coronal magnetic field, certain configurations of the magnetic fields may not favour reconnection. This should be the case, for instance, of an idealized situation where both the planets and the stellar magnetic field are perfectly aligned and with the same polarity. Therefore, it is possible that, due to the presence of the polarity reversals in the stellar magnetic field, radio emission from τ Boo b is an intermittent process.

While we have modelled the stellar wind that flows along the large-scale coronal magnetic field lines, the environment surrounding a star is likely to be much more dynamic, especially for a star such as τ Boo that is more active than the Sun (Maggio et al. 2011). We note that the radio flux estimated here is expected to increase if the planet is hit by powerful ejections of coronal material, e.g. caused by flares or coronal mass ejections.

5 DISCUSSION AND CONCLUSION

In this paper, we investigated the variation of the stellar wind in τ Boo during its cycle by means of three-dimensional numerical simulations. Our simulations adopt observationally derived surface magnetic field maps obtained at four different epochs. Because the stellar wind properties depend on the characteristics of the stellar magnetic field (geometry and intensity), the wind varies during the magnetic cycle of τ Boo.

We found that wind mass-loss rate varies little during the observed epochs of the cycle (less than 3 per cent), with a relatively more important variation in angular-momentum-loss rates (a factor of 2 during these epochs). The amount of (unsigned) open flux in the magnetic field lines shows a variation of up to a factor of 2.3 during the epochs studied here. The computed mass-loss rate for τ Boo is $\dot{M} \simeq 2.7 \times 10^{-12} \, M_\odot \, yr^{-1}$, two orders of magnitude larger than that of the solar wind. Angular-momentum-loss rates vary through the observed epochs and range from $\dot{J} \simeq 1.1$ to 2.2×10^{32} erg, which correspond to characteristic spin-down times $\tau \simeq 39$–78 Gyr, due to the stellar wind alone.

We also computed the EM from the quiescent closed corona, and found that it remains approximately constant through the cycle at a value of EM $\simeq 10^{50.6}$ cm^{-3}. This suggests that a magnetic cycle of τ Boo may not be detected by X-ray observations.

Although several efforts have been made towards detection of auroral radio emission from exoplanets, it has not been detected so far. Radio emission can be pumped by reconnection between the magnetic field lines of the stellar corona and the magnetosphere of the planet. Based on the analogy to the giant planets in the Solar system, which shows that radio emission scales with the kinetic and magnetic powers of the incident solar wind, we estimated radio emission from the hot Jupiter that orbits at 0.0462 au from τ Boo. We showed that, for a planet with a magnetic field similar to Jupiter ($B_p \simeq 14$ G), the radio flux is estimated to be about $\phi_{radio} \simeq 0.5$–1 mJy, occurring at an emission bandwidth of $\Delta f \simeq 34$ MHz. Although small, this emission bandwidth lies in the observable range of current instruments, such as LOFAR. However, we note that to observe such a small flux, an instrument with a sensitivity lying on a mJy level is required.[4] The same estimate was done considering the planet has a magnetic field similar to the Earth ($B_p \simeq 1$ G). Although the radio flux does not present a significant difference to what was found for the previous case, the emission bandwidth ($\Delta f \simeq 2$ MHz) falls at a range below the ionospheric cut-off, preventing its possible detection from the ground. In fact, we estimate that, due to the ionospheric cut-off at ∼10 MHz, radio detection with ground-based observations from planets with $B_p \lesssim 4$ G (equation 17, with $\Delta f = f_{cyc}$) should not be possible.

We remind the reader that in the estimate of radio emission, the lack of knowledge of some properties of the planet, such as its radius or its magnetic field intensity, and of the efficiency of the radio emission process, led us to make some assumptions, which were clearly stated in Section 4. Although we believe them to be reasonable hypotheses, they may incorporate uncertainties in our calculation, which we discuss next. (1) We assumed that the planet is about 1.3 times the size of Jupiter. The power emitted by the wind (which is converted in radio power) scales as the square of the size of the planet. Therefore, if we had assumed a planet radius of $1.58R_{Jup}$, the radio flux would increase about 50 per cent the values presented in this paper. (2) A second assumption, maybe the most uncertain one, is the efficiency ratio between the impacting wind power to the emitted radio power. In our estimates, we simply adopted the Solar system value of 10^{-5}, but this is an ad hoc assumption. Of course, a larger (smaller) efficiency value implies in a larger (smaller) radio flux. (3) We assumed that the emission bandwidth is $\Delta f = f_{cyc}$. Some authors adopt $\Delta f = f_{cyc}/2$ instead, which also could increase the radio flux by a factor of 2 (equation 18). (4) A fourth assumption that was implicit in our calculation is that the planet is magnetized, which may not be the case.

It is difficult to estimate errors involved in the calculated radio flux from τ Boo b, in especial due to reason (2). Although the detection of small fluxes, such as the ones found in this study, is certainly challenging, modern-day instruments, such as LOFAR, have great

---

[3] We demonstrate below that ϕ_{radio} weakly depends on the planetary magnetic field B_p for the parameters adopted. First, we note that α_0 correlates to B_p through equations (13) and (15) as $\sin \alpha_0 = (B_p^2/\mathcal{C})^{-1/12}$, where for the stellar winds simulated here, $\mathcal{C} \simeq 0.10$–0.16. This results in $\alpha_0 \simeq 32°$ for $B_p = 14$ G and $\alpha_0 \simeq 57°$ for $B_p = 1$ G. In addition, it is easy to see from equations (14) and (15) that $P_{radio} \propto P_k \propto r_M^2 \propto \sin^{-4} \alpha_0$. Substitution of the previous results, $\omega \propto (1 - \cos \alpha_0)$, equations (16) and (17) in (18), reveals that $\phi_{radio} \propto \sin^{-4} \alpha_0/[B_p(1 - \cos \alpha_0)(1 + 3 \cos^2 \alpha_0)^{1/2}] \propto (1 + \cos \alpha_0)(1 + 3 \cos^2 \alpha_0)^{-1/2}$, which has a weak dependence in α_0. For instance, for $32° \lesssim \alpha_0 \lesssim 57°$, the function $(1 + \cos \alpha_0)(1 + 3 \cos^2 \alpha_0)^{-1/2}$ is in the range [1.04, 1.12].

[4] The nominal noise level of LOFAR operating at 30 MHz, for an exposure time of 1 h is about 10 mJy. See details at http://www.astron.nl/radio-observatory/astronomers/lofar-imaging-capabilities-sensitivity/sensitivity-lofar-array/sensiti

potential to detect radio emission from exoplanets. Radio observation of τ Boo b is, therefore, a valuable exercise.

REFERENCES

Altschuler M. D., Newkirk G., 1969, Sol. Phys., 9, 131
Bastian T. S., Dulk G. A., Leblanc Y., 2000, ApJ, 545, 1058
Butler R. P., Marcy G. W., Williams E., Hauser H., Shirts P., 1997, ApJ, 474, L115
Catala C., Donati J.-F., Shkolnik E., Bohlender D., Alecian E., 2007, MNRAS, 374, L42
Cohen O., Drake J. J., Kashyap V. L., Hussain G. A. J., Gombosi T. I., 2010, ApJ, 721, 80
Cranmer S. R., Saar S. H., 2011, ApJ, 741, 54
Donati J.-F., Brown S. F., 1997, A&A, 326, 1135
Donati J.-F. et al., 2008a, MNRAS, 385, 1179
Donati J.-F. et al., 2008b, MNRAS, 386, 1234
Fares R. et al., 2009, MNRAS, 398, 1383
Farrell W. M., Desch M. D., Zarka P., 1999, J. Geophys. Res., 104, 14025
Grießmeier J.-M., Motschmann U., Mann G., Rucker H. O., 2005, A&A, 437, 717
Grießmeier J.-M., Preusse S., Khodachenko M., Motschmann U., Mann G., Rucker H. O., 2007a, Planet. Space Sci., 55, 618
Grießmeier J.-M., Zarka P., Spreeuw H., 2007b, A&A, 475, 359
Grießmeier J.-M., Zarka P., Girard J. N., 2011, Radio Sci., 46, 0
Hansen K. C., Ridley A. J., Hospodarsky G. B., Achilleos N., Dougherty M. K., Gombosi T. I., Tóth G., 2005, Geophys. Res. Lett., 32, 20
Jardine M., Cameron A. C., 2008, A&A, 490, 843
Jardine M., Collier Cameron A., Donati J., 2002, MNRAS, 333, 339
Jeffers S. V., Donati J.-F., Alecian E., Marsden S. C., 2011, MNRAS, 411, 1301
Keppens R., Goedbloed J. P., 1999, A&A, 343, 251
Keppens R., Goedbloed J. P., 2000, ApJ, 530, 1036
Lang P., Jardine M., Donati J.-F., Morin J., Vidotto A. A., 2012, MNRAS, submitted
Lazio T. J. W., Farrell W. M., 2007, ApJ, 668, 1182
Lazio T. J. W., Farrell W. M., Dietrick J., Greenlees E., Hogan E., Jones C., Hennig L. A., 2004, ApJ, 612, 511
Lazio T. J. W., Carmichael S., Clark J., Elkins E., Gudmundsen P., Mott Z., Szwajkowski M., Hennig L. A., 2010a, AJ, 139, 96
Lazio T. J. W., Shankland P. D., Farrell W. M., Blank D. L., 2010b, AJ, 140, 1929
Linde T. J., Gombosi T. I., Roe P. L., Powell K. G., Dezeeuw D. L., 1998, J. Geophys. Res., 103, 1889
Lugaz N., Manchester W. B., IV, Gombosi T. I., 2005, ApJ, 627, 1019
Maggio A., Sanz-Forcada J., Scelsi L., 2011, A&A, 527, A144
Manchester W. B., Gombosi T. I., Roussev I., De Zeeuw D. L., Sokolov I. V., Powell K. G., Tóth G., Opher M., 2004, J. Geophys. Res. (Space Phys.), 109, 1102
Marsden S. C., Donati J.-F., Semel M., Petit P., Carter B. D., 2006, MNRAS, 370, 468
Marsden S. C., Jeffers S. V., Donati J.-F., Mengel M. W., Waite I. A., Carter B. D., 2010, in Kosovichev A. G., Andrei A. H., Roelot J.-P., eds, Proc. IAU Symp. 264, Solar and Stellar Variability: Impact on Earth and Planets. Cambridge Univ. Press, Cambridge, p. 130
Matt S., Pudritz R. E., 2008, ApJ, 678, 1109
Meibom S. et al., 2011, ApJ, 733, L9
Mestel L., Selley C. S., 1970, MNRAS, 149, 197
Meyer-Vernet N., 2007, Basics of the Solar Wind. Cambridge Univ. Press, Cambridge

Morgenthaler A., Petit P., Morin J., Aurière M., Dintrans B., Konstantinova-Antova R., Marsden S., 2011, Astron. Nachr., 332, 866
Neubauer F. M., 1980, J. Geophys. Res., 85, 1171
Nichols J. D., 2011, MNRAS, 414, 2125
Opher M., Liewer P. C., Gombosi T. I., Manchester W., DeZeeuw D. L., Sokolov I., Toth G., 2003, ApJ, 591, L61
Opher M. et al., 2004, ApJ, 611, 575
Parker E. N., 1958, ApJ, 128, 664
Petit P., Dintrans B., Morgenthaler A., van Grootel V., Morin J., Lanoux J., Aurière M., Konstantinova-Antova R., 2009, A&A, 508, L9
Pinto R. F., Brun A. S., Jouve L., Grappin R., 2011, ApJ, 737, 72
Poppenhaeger K., Günther H. M., Schmitt J. H. M. M., 2012, Astron. Nachr., 333, 26
Powell K. G., Roe P. L., Linde T. J., Gombosi T. I., de Zeeuw D. L., 1999, J. Comput. Phys., 154, 284
Reiners A., Christensen U. R., 2010, A&A, 522, A13
Ridley A. J., de Zeeuw D. L., Manchester W. B., Hansen K. C., 2006, Advances Space Res., 38, 263
Roussev I. I. et al., 2003, ApJ, 595, L57
Russell C. T., Baker D. N., Slavin J. A., 1988, in Vilas F., Chapman C. R., Matthews M. S., eds, Mercury. University of Arizona Press, Tucson, p. 514
Saffe C., Gómez M., Chavero C., 2005, A&A, 443, 609
Sánchez-Lavega A., 2004, ApJ, 609, L87
Schwartz S. J., 1998, ISSI Sci. Rep. Ser., 1, 249
Shue J.-H., Song P., 2002, Planet. Space Sci., 50, 549
Stevens I. R., 2005, MNRAS, 356, 1053
Takeda G., Ford E. B., Stills A., Rasio F. A., Fischer D. A., Valenti J. A., 2007, ApJS, 168, 297
Tóth G., Kovács D., Hansen K. C., Gombosi T. I., 2004, J. Geophys. Res. (Space Phys.), 109, 11210
Valenti J. A., Fischer D. A., 2005, ApJS, 159, 141
Vidotto A. A., Opher M., Jatenco-Pereira V., Gombosi T. I., 2009a, ApJ, 699, 441
Vidotto A. A., Opher M., Jatenco-Pereira V., Gombosi T. I., 2009b, ApJ, 703, 1734
Vidotto A. A., Opher M., Jatenco-Pereira V., Gombosi T. I., 2010a, ApJ, 720, 1262
Vidotto A. A., Jardine M., Helling C., 2010b, ApJ, 722, L168
Vidotto A. A., Jardine M., Opher M., Donati J. F., Gombosi T. I., 2011a, MNRAS, 412, 351
Vidotto A. A., Jardine M., Helling C., 2011b, MNRAS, 414, 1573
Wood B. E., Müller H.-R., Zank G. P., Linsky J. L., 2002, ApJ, 574, 412
Wood B. E., Müller H.-R., Zank G. P., Linsky J. L., Redfield S., 2005, ApJ, 628, L143
Zarka P., 1998, J. Geophys. Res., 103, 20159
Zarka P., 2007, Planet. Space Sci., 55, 598
Zarka P., Treumann R. A., Ryabov B. P., Ryabov V. B., 2001, Ap&SS, 277, 293

APPENDIX A: DEPARTURE FROM POTENTIAL FIELD

The PFSSM (Altschuler & Newkirk 1969; Jardine et al. 2002) assumes that the magnetic field is everywhere potential, with a surface distribution of B_r derived from observed surface magnetic maps. The greatest advantage of this method is that the coronal magnetic field structure can be computed in a much smaller time-scale than the full MHD solution (for the cases run here, typically seconds versus days). However, a recurrent criticism that the PFSSM faces is that it may not correctly depict the structure of the magnetic field lines, which for instance may not be potential. With the aim of contrasting the results of our MHD modelling of the wind of τ Boo with the output of the PFSSM, which was used as the initial configuration for the magnetic field lines of our simulations, we compare the energy density of the magnetic field lines as derived by both methods.
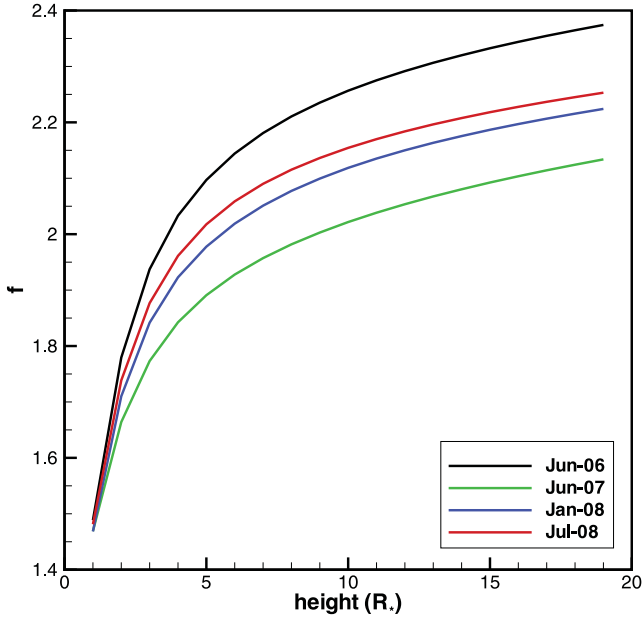
Figure A1. Ratio of the magnetic energy densities of the full MHD solution and the potential field solution (equation A2) as a function of height. We note that closer to the star, the MHD solution deviates little from the potential field solution, but this deviation becomes more important farther out from the star.

The stored magnetic energy contained in the potential field is in the lowest state, i.e. it is the minimum value of energy that the magnetic field lines can store. In the MHD wind case, excess energy is contained in the magnetic field lines due to stresses imposed by the wind. To quantify the departure of the MHD solution from the potential field solution, we evaluate the stored magnetic energy in each case. Defining the mean magnetic energy as

$$\langle B^2 \rangle = \frac{\int_{\mathcal{V}} B^2 \, \mathrm{d}\mathcal{V}}{\int_{\mathcal{V}} \mathrm{d}\mathcal{V}}, \qquad (A1)$$

where $\mathcal{V}$ is a given spherical volume, we calculated the ratio f between the energy contained in the MHD solution and the one in the PFSSM solution as

$$f = \frac{\langle B^2 \rangle_{\mathrm{MHD}}}{\langle B^2 \rangle_{\mathrm{PFSSM}}}. \qquad (A2)$$

Fig. A1 shows the fraction f as a function of stellar height for the cases we have simulated. To calculate the solution of the PFSSM, we assume that the source surface is located at $4R_\star$. We find that closer to the star, the MHD solution deviates little from the potential field solution. However, the departure from a potential field becomes more important farther out from the star. Note that at a height of $1R_\ast$ above the stellar surface, the stored magnetic energy density in the MHD solution is ~ 50 per cent larger than the magnetic energy density contained in the potential field solution (lowest energy state). At about a height of $5R_\ast$, $\langle B^2 \rangle_{\mathrm{MHD}}$ is about twice the value of $\langle B^2 \rangle_{\mathrm{PFSSM}}$.

APPENDIX B: CONSTRAINTS IMPOSED ON THE MAGNETIC FIELD RECONSTRUCTION

As the region of the star with latitudes $\lesssim -40°$ is hidden from the observer, the magnetic field there inevitably depends on assumptions involved in the reconstruction method. The surface magnetic field maps that are shown in Fig. 1 were obtained without assuming
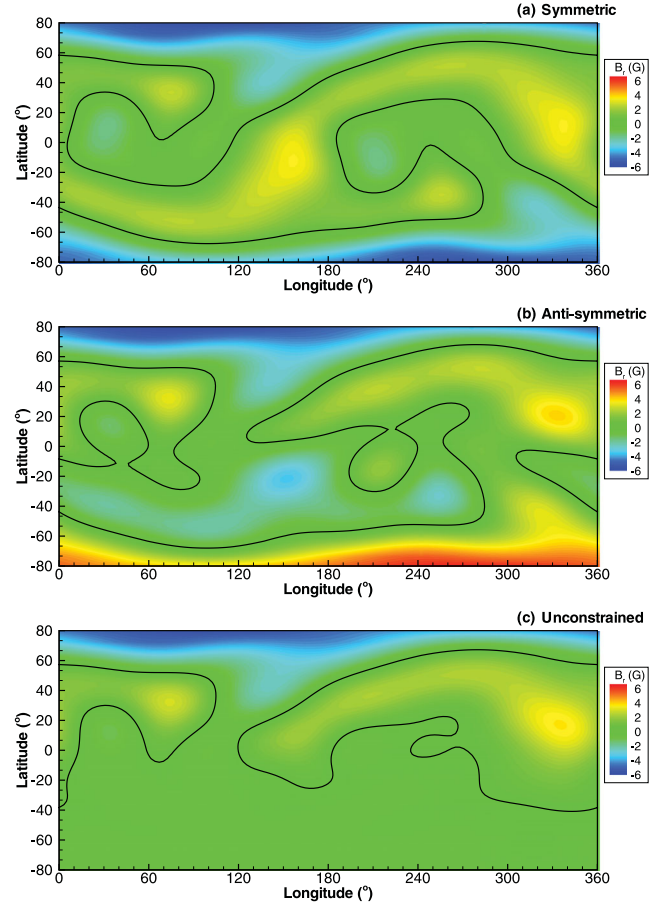

Figure B1. Surface distribution of the radial component of the magnetic field reconstructed from observations using ZDI and assuming that (a) the magnetic field is symmetrical with respect to the centre of the star, (b) antisymmetrical and (c) no constraints are adopted. The investigation shown here is done for the observing epoch of 2008 July. The colour-scale of all maps is adjusted to the maximum and minimum values of B_r for the antisymmetric case.

any constraints on the symmetry properties of the field. This results in (unsigned) magnetic field intensities in the unseen hemisphere that are much smaller and 'smoother' than the ones found in the visible hemisphere. Here, we investigate the sensitivity of our results with respect to this observational uncertainty. For that, we consider two different constraints on the properties of the magnetic field distribution that could have been applied during the reconstruction, if a physically motivated reason existed. In this investigation, we consider the observing epoch of 2008 July.

The first constraint assumes the magnetic field to be symmetrical with respect to the centre of the star. In that case, the solution obtained in the reconstruction pushes towards even orders of the multipole expansion (e.g. quadrupole). Fig. B1(a) shows the surface map that is derived once the symmetrical constraint is adopted. The second constraint adopts an antisymmetrical magnetic field (Fig. B1b), such that the solution essentially contains odd orders of the multipole expansion (e.g. dipoles, octopoles). For comparison, Fig. B1(c) shows the reconstructed image without adopting any constrains on the symmetry of the field (the same as shown in Fig. 1 but with a different colour-scale). As we can see, the reconstructions in the visible hemisphere remain approximately the same, but a different topology arises in the unseen hemisphere.

Table B1. Dependence of our results for 2008 July with respect to the assumptions adopted on the symmetrical properties of the field by the reconstruction method: unconstrained, symmetrical and antisymmetrical with respect to the centre of the star (column 1). The remaining columns are, respectively, the mass-loss rate ($\dot{M}$), angular-momentum-loss rate ($\dot{J}$), unsigned surface (Π_0) and open (Π_{open}) magnetic fluxes.

Assumption	$\dot{M}/10^{-12}$ ($M_\odot$ yr^{-1})	$\dot{J}$ (10^{32} erg)	Π_0 (10^{22} Mx)	Π_{open} (10^{22} Mx)
Unconstrained	2.68	1.1	1.14	9.0
Symmetric	2.67	1.4	1.94	12.2
Antisymmetric	2.69	1.4	1.97	12.2
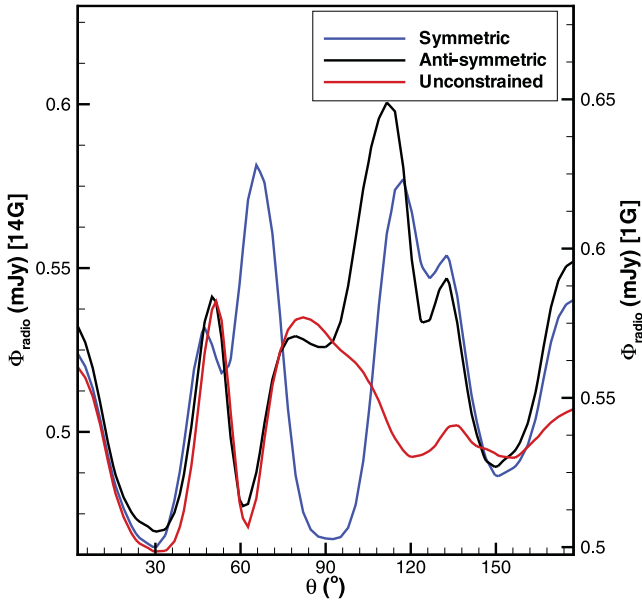
Figure B2. Radio flux estimated for τ Boo b (2008 July) as a function of colatitude θ, which is related to the unknown orbital inclination. The planet is either assumed to have a magnetic field intensity similar to the Earth (right axis) or similar to Jupiter's (left axis). Red solid curve assumes no constraints in the reconstruction of the surface magnetic field (red solid line in Fig. 7d), blue solid curve assumes symmetry with respect to the centre of the star and black solid curve assumes antisymmetry.

Using the magnetic maps presented in Fig. B1, we compute the stellar wind properties in the same way that was described in Section 3. Table B1 shows the relevant results of our investigation. We note that the unsigned magnetic flux at the surface of the star (Π_0), a direct output from the observations, is similar for both the symmetrical and antisymmetrical solutions, which are larger than the unconstrained option by a factor of 1.7. Similarly, we find that $\dot{J}$ and Π_{open} obtained are similar for the cases using the symmetrical and antisymmetrical maps, both of which are comparable to (although larger than) the values obtained using the unconstrained map. These similarities suggest that, for the parameters adopted in our model, the choice of the constraints adopted in the reconstruction of the surface magnetic field should not affect the stellar wind results obtained in this paper.

Using the results of the stellar wind simulations, we proceed to evaluate the exoplanetary radio emission as shown in Section 4. Fig. B2 shows the resultant radio flux emitted by a planet interacting with its host star's wind. The solid lines in Fig. B2 are labelled according to the assumption involved in the reconstruction of the stellar surface magnetic field. Because in the unconstrained case, the reconstructed magnetic field in the unseen hemisphere has smaller intensities and is less structured than that in the visible hemisphere, the stellar wind in the unseen region is less influenced by the latitude-dependent magnetic forces and, therefore, is more spherical. As a consequence, the exoplanetary radio emission is relatively 'flat' for a range of colatitudes from $\theta \sim 120°$ onwards (note that we omitted the region with $\theta \gtrsim 120°$ in Figs 6 and 7 due to the lack of information there). When the symmetric or antisymmetric assumptions are imposed, the more complicated topology of the magnetic field is reflected in the radio flux calculated for $120° \lesssim \theta \leq 180°$, as can be seen in Fig. B2 (compare blue and black lines against red one). In spite of that, there is no significant difference between the calculated radio fluxes (symmetric: 0.46–0.58 mJy; antisymmetric: 0.47–0.60 mJy; unconstrained: 0.46–0.59 mJy). This suggests that the choice of the constraints adopted in the reconstruction of the surface magnetic field should not affect the results obtained in this paper.

This paper has been typeset from a T$_E$X/L^{A}T$_E$X file prepared by the author.